Intraparticle Molecular Orbital Engineering of Semiconducting Polymer Nanoparticles as Amplified Theranostics for In Vivo Photoacoustic Imaging and Photothermal Therapy

Lyu, Yan; Fang, Yuan; Miao, Qingqing; Zhen, Xu; Ding, Dan; Pu, Kanyi

2016

https://hdl.handle.net/10356/80231

https://doi.org/10.1021/acsnano.6b00168

Intraparticle Molecular Orbital Engineering of Semiconducting Polymer Nanoparticles as Amplified Theranostics for *in vivo* Photoacoustic Imaging and Photothermal Therapy

Yan Lyu,[†] Yuan Fang,[‡] Qingqing Miao,[†] Xu Zhen,[†] Dan Ding,[‡] and Kanyi Pu[†],[*]

[†]School of Chemical and Biomedical Engineering, Nanyang Technological University, Singapore, 637457

[‡]State Key Laboratory of Medicinal Chemical Biology, Key Laboratory of Bioactive Materials, Ministry of Education, College of Life Sciences, Nankai University

Address correspondence to: kypu@ntu.edu.sg

ABSTRACT: Optical theranostic nanoagents that seamlessly and synergistically integrate light-generated signals with photothermal or photodynamic therapy can provide opportunities for cost-effective precision medicine, while the potential for clinical translation requires them to have good biocompatibility and high imaging/therapy performance. We herein report an intraparticle molecular orbital engineering approach to simultaneously enhance photoacoustic brightness and photothermal therapy efficacy of semiconducting polymer nanoparticles (SPNs) for *in vivo* imaging and treatment of cancer. The theranostic SPNs have a binary optical component nanostructure, wherein a near-infrared absorbing semiconducting polymer and an ultrasmall carbon dot (fullerene) interact with each other to induce photoinduced electron transfer upon light irradiation. Such an intraparticle optoelectronic interaction augments heat generation and consequently enhances the photoacoustic signal and maximum photothermal temperature of SPNs by 2.6- and 1.3-fold, respectively. Using the amplified SPN as the theranostic nanoagent, it permits enhanced photoacoustic imaging and photothermal ablation of tumor in living mice. Our study thus not only introduces a category of purely organic optical theranostics but also highlights a molecular guideline to amplify the effectiveness of light-intensive imaging and therapeutic nanosystems.

KEYWORDS: semiconducting polymer nanoparticles; theranostic; photoacoustic imaging; photothermal therapy

One of the emerging research areas at the convergence of physical science, engineering and life science is the development of theranostic nanoagents that integrate therapy and diagnosis for cost-effective precision medicine.[1-4] By virtue of the real-time diagnostic capability, theranostic systems can target accurately at refined therapeutic window, administering enhanced efficacy with minimized side effect.[5-7] As compared to magnetic,[8] ultrasound[9] and radioactive nanoparticles,[10,11] optical imaging agents have been more intensively integrated into theranostics,[12] probably because of the convenience that light is the solely-needed source not only providing the energy to afford diagnostic signals but also triggering the therapeutic processes such as photothermal therapy (PTT) and photodynamic therapy (PDT). Current optical theranostic systems generally rely on fluorescence as the signal readout and thereby share the drawbacks of autofluorescence background and limited light penetration depth, which unfortunately can compromise the diagnostic accuracy to some extent.[13,14]

Photoacoustic (PA) imaging as a new imaging modality exceeds the optical diffusion limit by detection of phonon instead of photon after light excitation, and thus provides deeper tissue penetration and higher spatial resolution for theranostics.[15] In addition, because PA signal is mainly determined by photothermal conversion, the principles of selecting agents for PA imaging are naturally consistent with those for PTT, which makes PA and PTT an ideal pair to be seamlessly and synergistically combined into theranostics.[16,17] Till now, many optical agents including small-molecule dyes,[18,19] porphysomes,[20-22] metallic nanoparticles,[23-27] carbon nanotubes[26,28-32] and 2D graphene analogs[33-37] have been used for PA/PTT theranostics, but each has its own unique advantages and disadvantages. For instance, organic dyes and metallic nanoparticles usually encounter the issue of poor photostability;[38,39] carbon nanotubes and

graphenes have broad PA spectra.[21,40] Thereby, new optical agents with improved properties are highly demanded so as to fully explore the potential of optical theranostics in medicine.

Semiconducting polymer nanoparticles (SPNs) have emerged as new optical nanomaterials that can be easily transformed from hydrophobic semiconducting polymers (SPs).[38,39,41-43] As SPs are completely organic and biologically inert, SPNs essentially circumvent the issue of heavy metal ion-induced toxicity to living organisms and thereby possess good biocompatibility.[44] In addition to their optical applications for *in vitro* cell imaging,[45-48] *in vivo* cell tracking,[49] targeted tumor imaging,[50,51] ultrafast hemodynamic imaging,[52] and drug toxicity evaluation,[41] we have recently revealed that SPNs can act as efficient PA imaging agents to permit ratiometric PA imaging of reactive oxygen species (ROS) in living mice.[39,41] We found that SPNs are resistant to ROS and much more photostable than gold nanorods and photoacoustically brighter than carbon nanotubes upon pulsed laser irradiation. Through investigation of the structure-property relationship of different diketopyrrolopyrrole-based SPs,[53] we have further confirmed that the PA brightness of SPNs is proportional to their photothermal conversion efficiency and thus envisioned their utility in PTT. In fact, polypyrrole (PPy)[54] and poly-(3,4- ethylenedioxythiophene):poly(4-styrenesulfonate)[55] based SPNs have been reported for PTT, but their PTT efficacies were constrained by their weak absorption in the near-infrared (NIR) region as their absorption maxima are located in the visible region. Moreover, PA/PTT theranostic systems based on SPNs have been less studied.[53,56,57] Although synthesis of new SPs is certainly a feasible way to improve both PA imaging and PTT of SPNs, it inevitably requires a huge input of time and effort. Thereby, simple yet effective approaches toward efficient PA/PTT theranostic systems based on SPNs remain elusive.

We herein report an intraparticle molecular orbital engineering approach to enhance both PA brightness and PTT efficiency of SPNs for amplified theranostics in living mice. The designed theranostic SPNs are binary, within which the primary SP and the secondary optical dopant play their roles as electron donor and acceptor, respectively. The molecular orbitals of the optical components are carefully aligned to make the electron affinity and ionization potential of the SP respectively higher than those of the dopant. Such an energy level alignment favors photoinduced electron transfer (PET) within the confined nanocompartment and thus results in quenched fluorescence and enhanced non-radiative heat generation after light irradiation, ultimately bringing in both amplified PA brightness and improved PTT efficiency. The synthesis and characterization of theranostic SPNs are first described, followed by *in vitro* validation of our intraparticle molecular orbital engineering concept through systematic investigation of the effect of dopant on the optical, PA and PTT properties of SPNs. At last, the proof-of-concept application of theranostic SPNs in imaging and treatment of tumor in living mice is demonstrated.

RESULTS AND DISCUSSION

The theranostic SPNs were synthesized through nanoprecipitation. Poly[2,6-(4,4-bis-(2-ethylhexyl)-*4H*-cyclopenta[2,1-b;3,4-b']dithiophene)-*alt*-4,7-(2,1,3-benzothiadiazole)] (PCPDTBT) and (6,6)-phenyl-C71-butyric acid methyl ester (PC70BM) (**Figure 1**) were chosen as the primary component and the secondary dopant, respectively. PCPDTBT is a SP with a relative narrow energy band gap, ensuring the strong absorption of NIR light.[58] PC70BM is a fullerene with highly electrophilicity and hydrophobicity,[59] which can be efficiently encapsulated into the nanoparticle to closely contact with PCPDTBT. The highest occupied molecular orbital (HOMO) and lowest unoccupied molecular orbital (LOMO) are -4.9 and -3.5 eV for PCPDTBT

and -6.5 and -4.3 eV for PC70BM, respectively.[60] Thereby, the energy levels of these optical pairs are ideally aligned to favor intraparticle PET. The amphiphilic triblock polymer (PEG-*b*-PPG-*b*-PEG) is used to improve the hydrophilicity of SPNs as well as to provide a relatively inert particle surface.

Figure 1. Schematic illustration of intraparticle molecular orbital engineering design approach for amplified photoacoustic (PA) imaging and photothermal therapy (PTT). (**a**) Chemical structures of PCPDTBT, PC70BM and PEG-*b*-PPG-*b*-PEG. (**b**) Photography of the solutions of SPNs with the different doping amount of PC70BM ($_{w/w}$%). [SPN] = 16 μg/mL. (**c**) Illustration of PET-induced amplified theranostic SPNs. The highest occupied molecular orbital (HOMO) and lowest unoccupied molecular orbital (LUMO) are -4.9 and -3.5 eV for PCPDTBT and -6.5 and -4.3 eV for PC70BM.

To optimize the doping amount for optical theranostics, SPNs with the different doping amount of PC70BM were prepared: SPN-F0, SPN-F4, SPN-F10, SPN-F20 and SPN-F40, which have the weight percentages of PC70BM equal to 0 $_{w/w}$%, 4 $_{w/w}$%, 10 $_{w/w}$%, 20 $_{w/w}$%, and 40 $_{w/w}$%, respectively. As shown in **Figure 1**b, all the nanoparticle solutions are transparent and

have the quite similar color of cyan. Dynamic light scattering (DLS) shows that the SPNs possess the similar average diameter ~50 nm (**Figure 2**c and Figure S1 in the Supporting Information). Thereby, the PC70BM doping has a negligible effect on the size of SPNs, due to the ultrasmall size of PC70BM (~1 nm).[61] Using SPN-F20 as an example, transmission electron microscopy (TEM) shows a spherical morphology with the diameter of ~38 nm (**Figure 2**a). The TEM-measured diameter is smaller than that measured by DLS (54.33 ± 0.55 nm) (**Figure 2**b), which should be attributed to the shrinkage of nanoparticles during the sample preparation of TEM. After being stored in the dark place at room temperature (24 °C) for 44 days, the size of SPN-F20 remained nearly the same (Figure S2, Supporting Information). In addition, the PL spectrum of SPN-F20 shows no obvious change after incubation in serum at 37°C for 24 h (Figure S3, Supporting Information). These data prove the excellent stability of fullerene-doped SPNs.
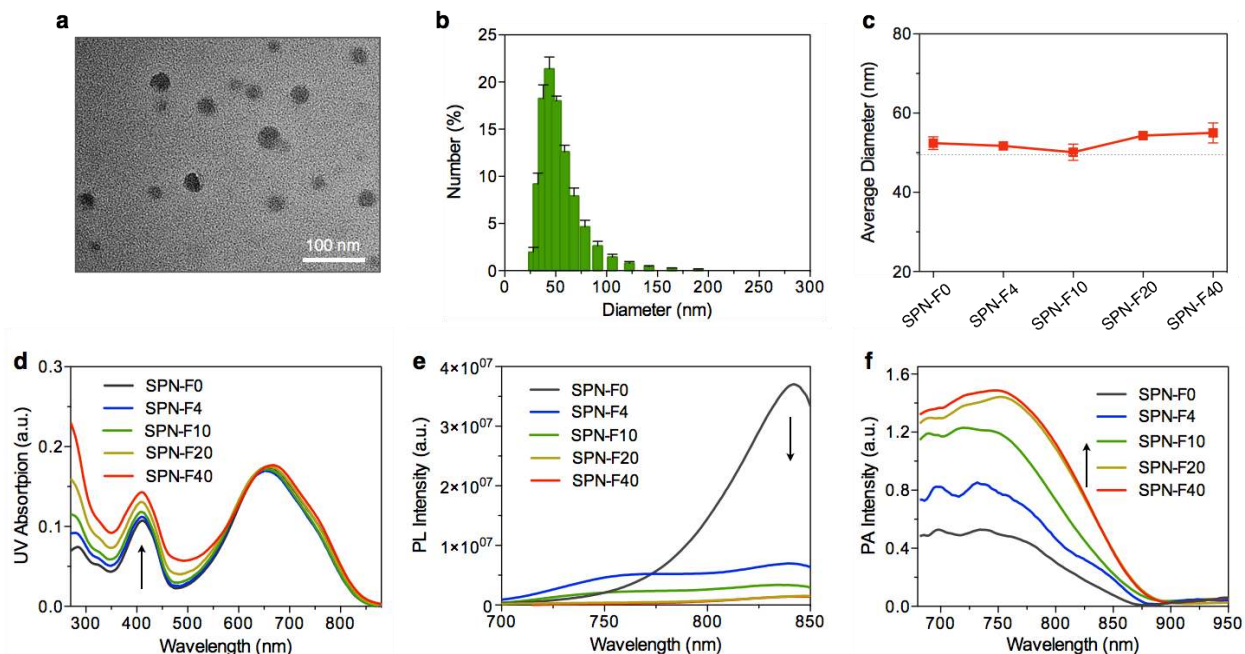
Figure 2. *In vitro* characterization of SPNs. Representative TEM images (**a**) and DLS (**b**) of SPN-F20. (c) Hydrodynamic average diameters of SPNs with different doping amount of PC70BM. UV-vis absorption (**d**), PL (**e**) and photoacoustic spectra (**f**) of SPNs. [SPN] = 2 μg/mL. 1×PBS (pH 7.4). Excitation for PL: 650 nm. The arrows indicate the increase (d&f) or decrease (e) of the intensities with the increased doping amount of PC70BM in SPNs.

To study the doping effect on optical properties, we measured and compared the UV-Vis absorption, photoluminescence (PL) and PA spectra of these SPNs in PBS at pH 7.4. As shown in **Figure 2**d, the non-doped nanoparticle of SPN-F0 has two absorption peaks with the maxima at 404 and 650 nm, respectively. With increasing the doping amount of PC70BM, the peak at 404 nm gradually elevates, while the peak at 650 nm remains unchanged. Such an increase at 404 nm is caused by the contribution from PC70BM which has broad absorption spectrum from 200 to 550 nm.[62] The PL spectrum of SPN-F0 has a maximum emission at 840 nm (**Figure 2**e), which is gradually quenched with increasing doping amount of PC70BM. In contrast, the physical mixture of SPN-F0 and PC70BM does not show such a fluorescence quenching and the PL intensity of SPN-F0 remains the same regardless of the concentration of PC70BM (Figure S4 in the supporting information). This not only proves the doping of PC70BM into the SPN but also confirms the efficient intraparticle PET process from PCPDTBT to PC70BM. It should be noted that the PL is completely quenched at the doping amount of 20 w/w%. The PA spectra of SPNs were acquired by pulsed laser irradiation ranging from 680 to 950 nm (**Figure 2**f). All the SPNs show detectable PA signals ranging from 680 to 825 nm. With increasing the doping amount of PC70BM, the PA intensity gradually increases while the peak at around 750 nm progressively dominates. This subtle spectral change is in line with the slightly red-shifted spectral profile and the increased vibronic shoulder at 750 nm in the absorption spectra of these SPNs. The difference between the absorption spectral profile and PA spectral profile of SPNs

should be mainly caused by two facts: (i) optical absorption and PA spectra measures different photophysical processes; and (ii) optical illumination parameters are different, high-power pulsed laser for PA spectra verse low-power continuous-wave light illumination for absorption spectra.

The doping effect on the fluorescence brightness, PA brightness and PT efficiency was investigated and compared for the different SPNs in PBS (pH 7.4) at the same concentration. As shown in **Figures 3**a-c, epi-fluorescence, PA, and PT images of the SPNs solutions were recorded by IVIS living imaging system, Endra PA tomography system and IR camera, respectively. The intensities and the temperatures were quantified and summarized in **Figures 3**d-f. With increasing the doping amount of PC70BM, the fluorescence intensity drops rapidly, the PA intensity increases obviously, and the solution temperature increases gradually. It should be emphasized that the fluorescence intensity of SPN-F20 is very close to the background noise, while its PA intensity and the solution temperature are as high as those of SPN-F40. The data thus points out that the optimum doping amount of PC70BM is 20 $_{w/w}$%. As compared to SPN-F0, the PA intensity of SPN-F20 is amplified by 2.6 fold, while its solution temperate after laser irradiation for 5 min is elevated by 1.3-fold from 48 to 62°C. The tendencies of fluorescence brightness, PA brightness and PT efficiency upon increasing the doping amount of PC70BM coincide well with each other and comply with the photophysical mechanisms. As well known, the excitation energy absorbed by a chromophore is generally dissipated through the following pathways: i) fluorescence emission, ii) generation of heat through vibrational relaxation (thermal deactivation), and iii) intersystem conversion to long-lived species (*e.g.*, phosphorescence).[63] As these SPNs are not detectably phosphorescent, the pathways (i) and (ii) play the roles in determining their fluorescence, PA and PT efficiencies. Upon light excitation, the thermal

deactivation competes with light emission in determining heat and acoustic generation. As a consequence, the loss of fluorescence intensity induced by intraparticle PET within SPNs is spontaneously accompanied by the gain of amplified PA brightness and increased solution temperature. These *in vitro* data firmly predict that as compared to SPN-F0, SPN-F20 should be a better optical theranostic system for PA imaging and PTT.
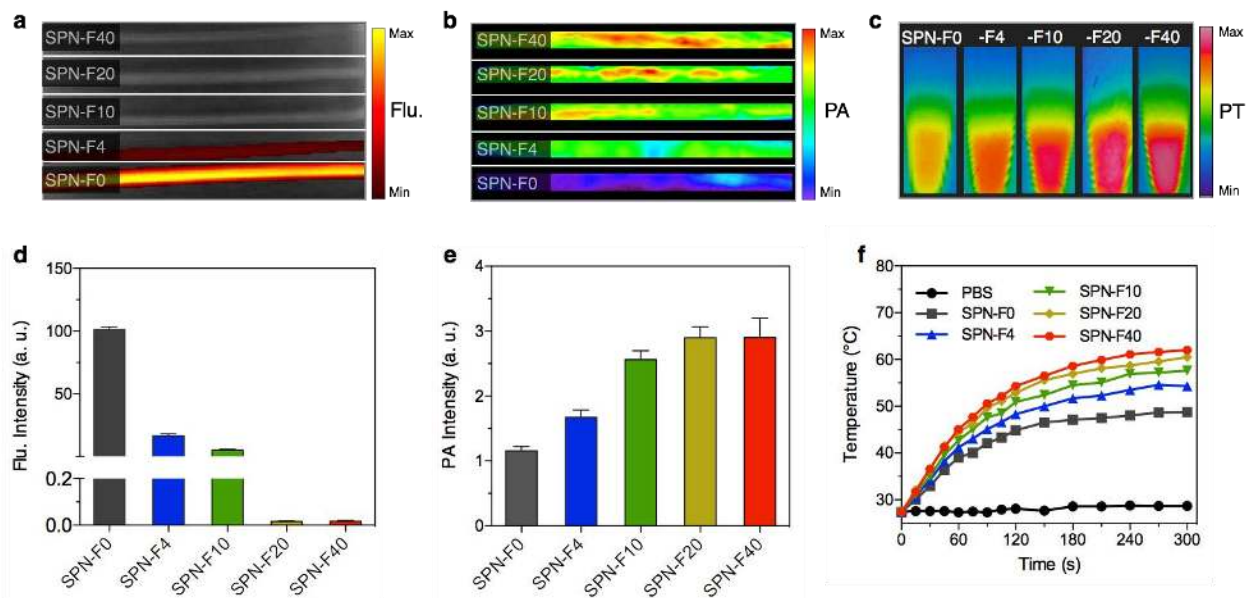

Figure 3. *In vitro* fluorescence, PA and PT data of SPNs. Epi-fluorescence (**a**) and PA (**b**) images of SPN solutions in tubes; IR thermal images of SPN solutions after laser irradiation for 300 s (**c**). Quantification of fluorescence (**d**) and PA (**e**) intensities of SPNs in solutions; (**f**) The temperature of SPN solutions as a function of laser irradiating time at the power intensity of 0.5 W/cm^2. [SPN] = 15 μg/mL, 1×PBS (pH 7.4). A single laser pulse at 680 nm with a laser fluence of 9 mJ/cm^2 and a pulse repetition rate of 20 Hz was used for photoacoustic imaging. The fluorescence images were acquired by excitation at 665 nm and collection of signals at 840 nm. Error bars were based on standard error of mean (SEM) (n = 3).

The diagnostic capability of the theranostic SPNs was validated with xenograft 4T1 tumor mouse model. Among these SPNs with the different doping amount of PC70BM, SPN-F20 was tested along with the nondoping control nanoparticle (SPN-F0) as SPN-F20 has the best PA and

10

PT efficiencies. After systemic administration of SPN-F20 or SPN-F0 into the tumor-bearing mice through tail vein, the PA images were recorded overtime by pulsed laser excitation at 750 nm. The PA signals reach its maximum at 6 h post-injection for both SPNs, consistent with the *in vivo* epi-fluorescence imaging results (Figure S5 in the Supporting Information). The PA images at t=6 h and the PA intensity as a function of post-injection time are shown in **Figure 4**a and **4**b, respectively. Generally, the SPN-F20 injected mice have much higher PA intensities in the tumor area as compared to that for SPN-F0 at all the time points. At t=6 h, the PA intensity reaches its maximum for both SPNs, where the intensity for SPN-F20 injected mice is 1.8-fold of that for SPN-F0 treated mice. This intensity difference can be obviously visualized in the PA images (**Figure 4**a). The amplified PA brightness of SPN-F20 allows us to carry out a 3D signal reconstruction, which clearly delineates that the PA signals are detectable both inside and outside of the blood vessels of tumor. The almost homogeneously-distributed PA signal proves the extravasation ability of SPN-F20, which is frequently observed for SPNs as reported in our previous studies.[51] The *ex vivo* PA data in **Figure 4c** illustrate that SPN-F20 and SPN-F0 have quite similar dynamic biodistribution in major organs such as tumor, liver, spleen and skin *et al.*. Such a similarity for different SPNs stems from their nearly identical particle sizes (~50 nm) and the same PEG-coated surface structure, suggesting the probability of using SPNs for multiplex *in vivo* imaging provided that their PA maxima are turned to different laser wavelengths.
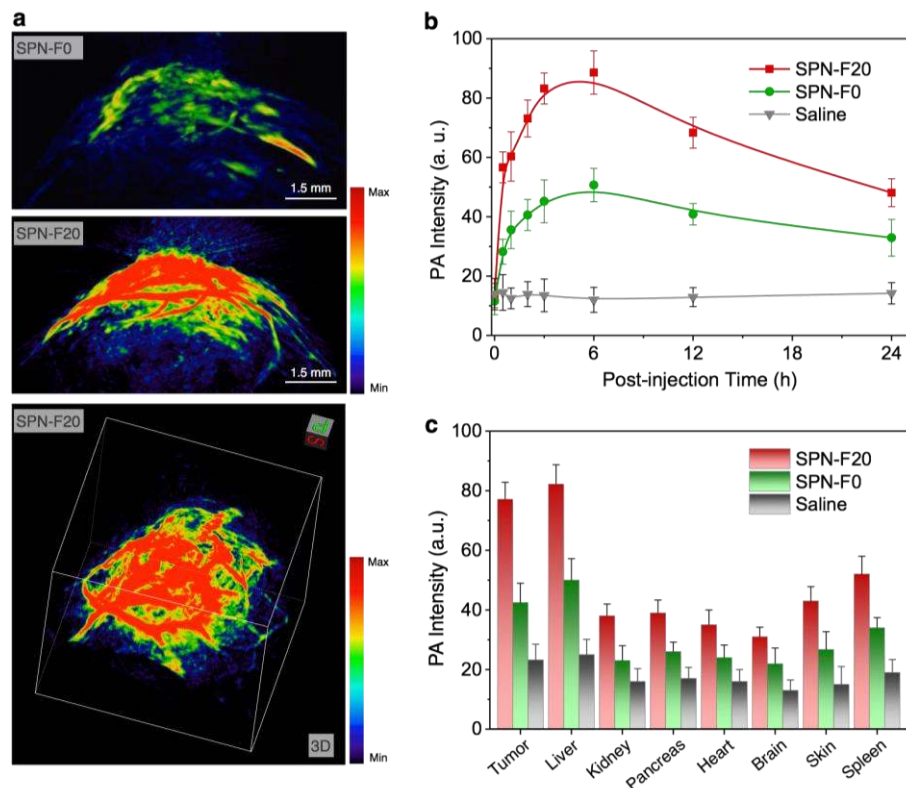
Figure 4. *In vivo* **photoacoustic imaging.** (**a**) PA images of tumor after systemic administration of SPN-F0, SPN-F20 (200 μL, 100 μg/mL) or saline, for 6 h. The representative PA maximum intensity projection (MIP) images with axial view for SPN-F0 and SPN-F20 and the 3D image for SPN-F20. (**b**) Quantification of PA intensities at 750 nm as a function of post-injection time of SPN-F0, SPN-F20 or saline. (**c**) *Ex vivo* PA quantification of major organs of mice 24 h after systemic administration of SPNs or saline. The PA data were acquired at 750 nm. The weigh for the part of each organ used for PA measurement is 100 mg. Error bars were based on standard error of mean (SEM). (n = 4).

The therapeutic capability of the theranostic SPNs was testified on xenograft 4T1 tumor mouse model using SPN-F20 and SPN-F0 as examples. According to the PA imaging results, PTT was conducted at 6 h post-injection of SPNs as this time point shows the highest PA signals (**Figure 4**b). After systemic administration of SPN-F20, SPN-F0 or saline for 6 h, the 4T1-tumor bearing mice were irradiated under the laser of 808 nm with the power of 0.3 W/cm^2 for 5 min. The thermal images of mice and the surface temperature of tumor as a function of laser irradiation

12

time are shown in **Figure 5**a and **5**b, respectively. It is clear that the tumor temperature of SPN-F20 injected mice is higher than that for both SPN-F0 and saline injected mice at all the time points. The tumor temperature reaches plateau after laser irradiation for 2 min. At this time point, the tumor temperature of SPN-F20 injected mice is 62°C, which is 1.3- and 1.7-fold of that for SPN-F0 (48°C) and saline (37°C) injected mice, respectively. Such a difference in the tumor temperature under laser irradiation is consistent well with the *in vitro* data (**Figure 3**f), which also shows 1.3-fold temperature enhancement when changing from SPN-F0 to SPN-F20 (**Figure 3**f).

To qualitatively evaluate the ablating effect of theranostic SPNs, the tumor sizes were continuously monitored for 16 days after PTT (**Figure 5**c & Figure S6 in the Supporting information). Without laser irradiation, the tumors of SPNs injected mice grew as quickly as that of saline injected mice, indicating that both SPNs themselves do not have the ability to inhibit tumor growth. In contrast, after laser irradiation, both SPNs effectively inhibited the tumor growth for the first 8 days. However, only SPN-F20 successfully inhibited the tumor growth, while SPN-F0 failed to do so at later time points. The better PTT outcome for SPN-F20 can be contributed to the fact that the tumor temperature of SPN-F20 injected mice increased to 62°C, while SPN-F0 injected mice was only able to reach 48°C, which was not high enough to effectively ablate the cancer cells *in vivo* under our experiment conditions. Moreover, the body weights of the mice for all groups were continuously monitored for 16 days after PTT, and no significant weight loss was observed (**Figure 5**d), suggesting the low toxicity of all treatments. This is consistent with the *in vitr*o data showing the high cytocompatibility of SPNs (Figure S7 in the Supporting Information).
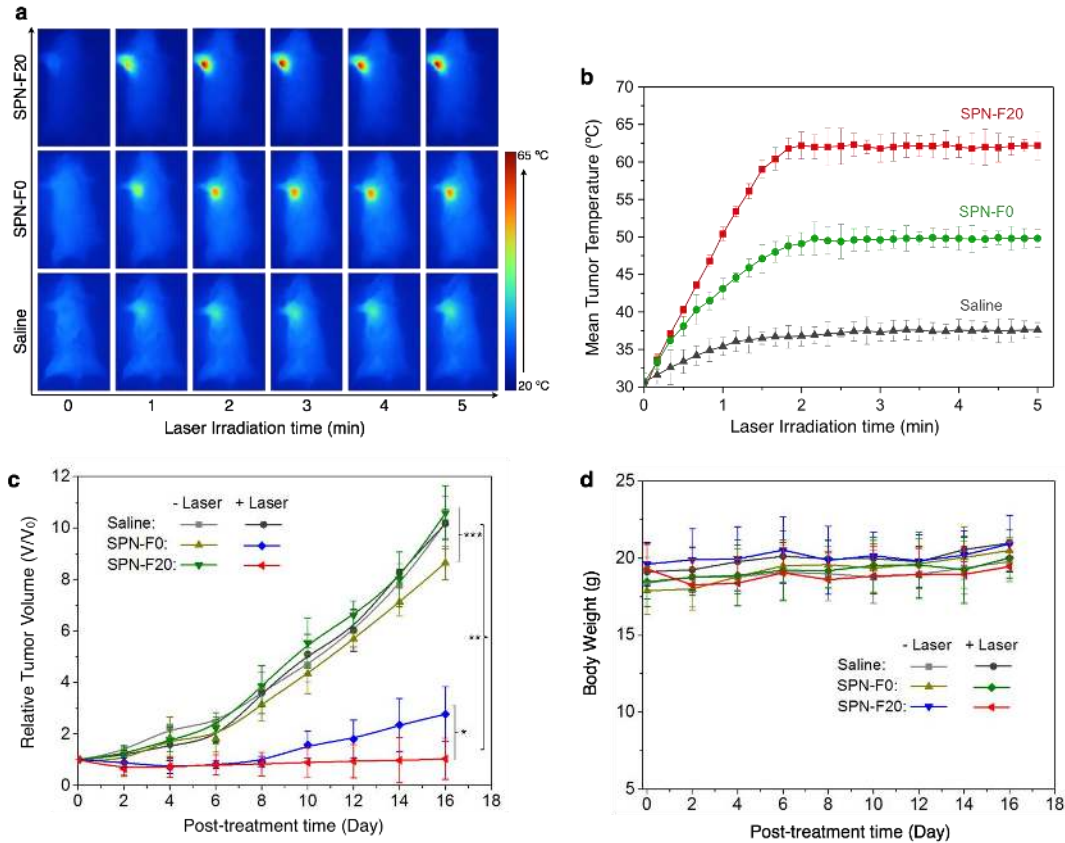
Figure 5. *In vivo* **photothermal therapy**. (**a**) IR thermal images of 4T1 tumor-bearing mice under 808 nm laser irradiation ($0.3\ W/cm^2$) after systemic administration of saline, SPN-F0 or SPN-F20 (200 μL, 100 μg/mL) at post-injection time of 6 h. (**b**) Mean tumor temperature as a function of laser irradiation time after systemic administration of saline, SPN-F0 or SPN-F20 at post-injection time of 6 h. Error bars were based on standard error of mean (SEM). (n = 4). (**c**) Tumor growth curves of different groups of mice after systemic treatment with saline, SPN-F0 or SPN-F20 with and without laser irradiation. Error bars were based on standard error of mean (SEM). ([*] indicate $p < 0.05$, [**] indicates $p < 0.01$, [***] indicates $p > 0.05$, n = 4). (**d**) Body weight data of mice after systemic treatment with saline, SPN-F0 or SPN-F20 with and without laser irradiation. Error bars were based on standard error of mean (SEM) (n = 4).

To further verify the therapeutic outcome of theranostic SPNs, all the groups were sacrificed at day 16 and histological analysis was performed for different organs using hematoxylin and eosin (H&E) staining as well as fluorescent proliferating cell nuclear antigen (PCNA) and TdT-

mediated dUTP-biotin nick end labeling (TUNEL) staining. As shown in **Figure 6**a, no noticeable histopathological abnormities or lesions can be found for the liver and spleen of both SPN-F20 and SPN-F0 injected mice after PTT. In contrast, typical nucleus dissociation is observed for the tumor tissues for SPNs-injected mice after PTT. Besides, both superficial and deep tumor tissues of SPN-F20 injected mice show more obvious necrosis as compared to those of SPN-F0 injected mice. The analysis of large H&E images (Figures S8 in the Supporting Information) shows that the percentage of necrosis area of SPN-F20 in the whole image is 77.2%, which is significantly higher than that for SPN-F0 (42.9%) and saline (2.1%).

The PCNA fluorescence staining in **Figure 6**b indicates that the reproduction capacity is obviously reduced for SPNs-injected mice after PTT; however, some green fluorescent spots can still be found in the deep tumor tissue of SPN-F0 injected mice. Similarly, the TUNEL fluorescence staining shows that apoptosis is clearly detectable for SPNs-injected mice after PTT, while SPN-F20 causes severer apoptosis than SPN-F0 does as witnessed by the stronger green fluorescence from the TUNEL staining for both superficial and deep tumor tissues of SPN-F20 injected mice. It should be noted that no obvious apoptosis and necrosis as well as reduced reproduction capacity are observed for all the control groups (without laser irradiation or saline injected mice with laser irradiation, Figures S9&S10 in the Supporting Information). These histological data verify at cellular level that SPN-F20 has a better PTT efficacy than SPN-F0 does, which is in perfect accordance with the *in vivo* observation from the tumor growth curves in **Figure 5**c.
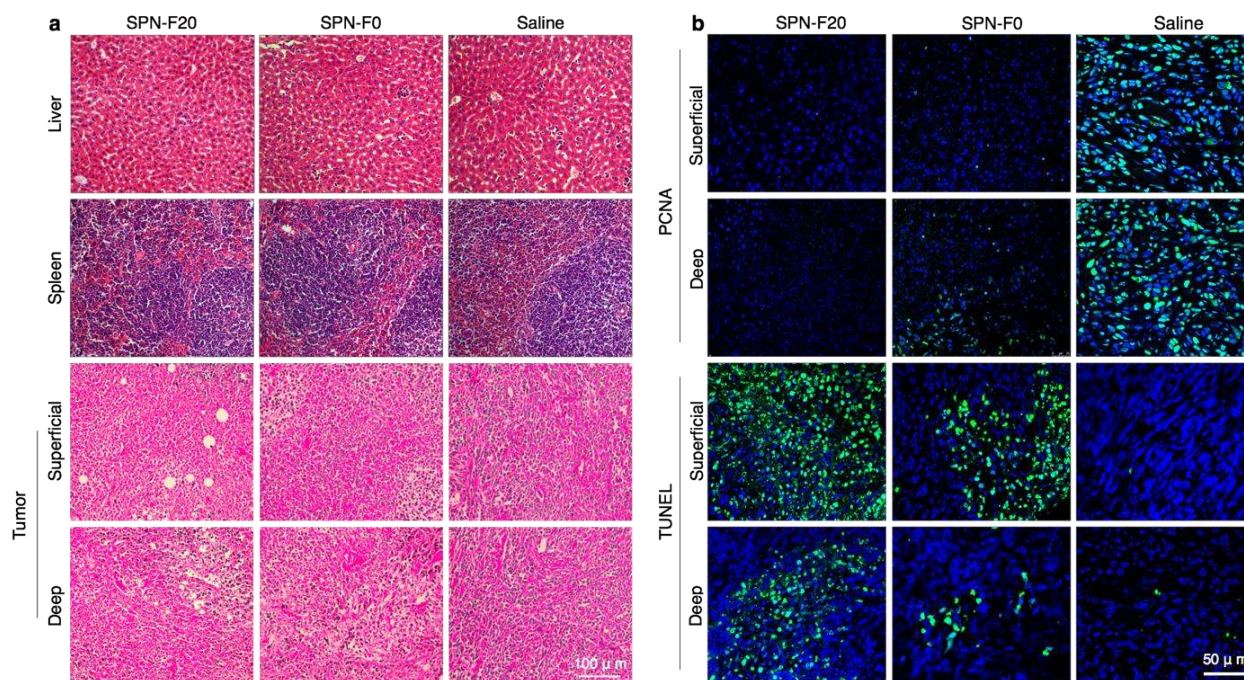
Figure 6. (**a**) Histological H&E staining for liver, spleen and tumors (superficial & deep regions) at Day 16 after the photothermal treatment with saline, SPN-F0 or SPN-F20. (**b**) Fluorescence PCNA and TUNEL staining of tumor slices (superficial & deep regions) at day 16 after the photothermal treatment with saline, SPN-F0 or SPN-F20. Green fluorescence indicates the signal from PCNA and TUNEL staining while the blue fluorescence is from the nucleus staining.

CONCLUSIONS

We have demonstrated an intraparticle molecular orbital engineering approach to develop organic optical theranostics with amplified PA brightness and PTT efficacy. Our design capitalizes on the structural flexibility and synthetic simplicity of SPNs to create intraparticle PET by incorporation of an electron-withdrawing carbon dot (fullerene: PC70BM) into SPNs. Such an intraparticle electronic interaction between SP and PC70BM results in enhanced heat generation upon light irradiation, subsequently amplifying both PA brightness and PTT efficacy for the theranostic SPNs. As compared to the non-doped SPN (SPN-F0), the *in vitro* PA brightness of the doped SPN (SPN-F20) is amplified by 2.6-fold, while its maximum

photothermal temperature increases by 1.3-fold from 48 to 62°C both *in vitro* and *in vivo*. Due to the ultrasmall size of PC70BM, doping has no obvious impact on the particle size, and thus the theranostic SPNs have similar bio-distribution. As confirmed by both *in vivo* and *ex vivo* histological data, utilization of SPN-F20 as the optical theranostics permits enhanced PA imaging and improved photothermal ablation of tumor in living mice. By virtue of their completely organic ingredients, the theranostic SPNs show no sign of toxicity both *in vitro* and *in vivo* and thus hold great promise for other therapeutic applications.

As the energy levels of optically active components within nanoparticles can be easily paired and aligned to favor PET, the design concept of amplified optical theranostics should be applicable to other systems. For instance, integration of graphene and SP should have the similar synergistic outcome due to the widely observed PET-induced fluorescence quenching for them.[64] Thus, our study not only brings in a new generation of organic optical theranostics based on SPNs but also provides new molecular design guidelines to seamlessly and synergistically merge light-intensive imaging with therapeutic applications.

METHODS

Chemicals. All chemicals were purchased from Sigma-Aldrich unless otherwise stated.

Materials Characterization. TEM images were obtained on a JEM 1400 transmission electron microscope with an accelerating voltage from 40 to 120 kV. Dynamic light scattering (DLS) was performed on the Malvern Nano-ZS Particle Sizer. UV-Vis spectra were recorded on a Shimadzu UV-2450 spectrophotometer. Fluorescence measurements were carried out on a Fluorolog 3-TCSPC spectrofluorometer (Horiba Jobin Yvon). Fluorescence images of SPNs solutions were acquired with the IVIS spectrum imaging system. IR thermal image was recorded by the

photothermal camera FLIR T420. Fluorescence confocal image was conducted using confocal laser scanning microscopy (Leica TSC SP8, Germany). A 808 nm high power NIR Lasers (operating mode: CW, output power after fiber: 2.5 W, LED display: diode current, multimode fiber, fiber core diameter: 400 µm, fiber connector: SMA905, with tunable laser driver module: 0 - 100%) purchased from CNI Co., Ltd. was used for PTT experiments. The laser spot size is 1 cm^2. It was used as the surface laser and position on top of the mice. The laser power was measured by laser power meter.

Preparation of SPNs. PCPDTBT (1 mg) and PC70BM (1 mg) were dissolved in THF (1 mL) individually by bath sonication to get the solution of 1 mg/mL. The resulted solutions were filtered through a polyvinylidene fluoride (PVDF) syringe driven filter (0.22 µm) (Millipore). Then, a mixed THF solution (1 mL) containing PCPDTBT (0.25, 0.24, 0.225, 0.20, 0.15 mg/mL), corresponding to PC70BM (0, 0.01, 0.025, 0.05, 0.10 mg/mL according to the doping amount) and PEG-*b*-PPG-*b*-PEG (20 mg/mL) were used to prepare SPNs by rapidly injecting the mixture into distilled-deionized water (9 mL) under continuous sonication with a microtip-equipped probe sonicator (Branson, W-150) at a power output of 6 watts RMS for 2 min. After sonication for additional 1 min, THF was evaporated at 65°C under nitrogen atmosphere. The aqueous solution was filtered through a polyethersulfone (PES) syringe driven filter (0.22 µm) (Millipore), and washed three times using distilled-deionized water and 50K centrifugal filter units (Millipore) under centrifugation at 3,500 rpm for 15 min at 4°C. The SPNs solutions were diluted in 1× PBS buffer (pH 7.4) and the concentrations were determined by UV-Vis absorption according to absorption coefficients of PCPDTBT. The SPNs solutions were finally concentrated to 0.08 mg/mL (based on the mass of PCPDTBT) by ultrafiltration and stored in dark at room temperature. The actual doping amount of PC70BM has been calculated according to the

extinction coefficients of PC70BM at 404 nm and the SP (PCPDTBT) at 650 nm. The actual doping amount of SPN-F0, SPN-F4, SPN-F10, SPN-F20, SPN-F40 are 0 w/w%, 9.46 w/w%, 18.73 w/w%, 33.27 w/w%, and 42.95 w/w%, respectively. The actual doping amount for each SPNs thereby is very close to the feeding amount.

PA Instrumentation. A commercial Endra Nexus128 PA tomography system (Endra Inc., Ann Arbor, Michigan) was also used in this study. The system houses a tunable nanosecond pulsed laser (7 ns pulses, 20 Hz pulse repetition frequency, 9 mJ/pulse on the animal surface, wavelength range (680−950 nm), 128 unfocused ultrasound transducers (with 5 MHz center frequency and 3 mm diameter) arranged in a hemispherical bowl filled with water, animal tray on top of the bowl, data acquisition/reconstruction console, servo motors for 3D rotation of the bowl, and a temperature monitor of the water bath.

In vitro **PTT of SPNs**. The 1×PBS solution (pH 7.4) of SPNs (200 μL, 15 μg/mL) and the same amount of PBS buffer were exposure to laser of 808 nm (0.5 W/cm^2). The temperature was recorded every 15 seconds and stopped until the temperature without big changes (5 minutes here).

Cell Culture. HeLa cervical adenocarcinoma epithelial cells were purchased from the American Type Culture Collection (ATCC). HeLa cells were cultured in DMEM (Dulbecco's Modified Eagle Medium) (GIBCO) supplemented with 10% FBS (fetal bovine serum) (GIBCO) and antibiotics (10 U/mL penicillin and 10 mg/mL streptomycin). The cells were maintained in an atmosphere of 5% CO_2 and 95% humidified air at 37°C.

Cytotoxicity Test. Cells were seeded in 96 well plates (1000 cells in 100 μL per well) for 24 h, and then SPN-F0 and SPN-F20 (final concentration 5, 10, and 15 μg/mL) was added to the cell culture medium separately. Cells were incubated with SPN-F0 or SPN-F20 for 24 h, followed by

the addition of MTT (20 µL, 5 mg/mL) for 3 h. The media was removed and DMSO (200 µL) was added into each well and gently shaken for 10 min at room temperature to dissolve all formed precipitates. The absorbance of MTT at 550 nm was measured by using a SpectraMax M5 Microplate/Cuvette Reader. Cell viability was expressed by the ratio of the absorbance of the cells incubated with SPN-F0 or SPN-F20 solution to that of the cells incubated with culture medium adding the same volume of saline.

Tumor Mouse Model. All animal studies were performed in compliance with the guidelines set by Tianjin Committee of Use and Care of Laboratory Animals and the overall project protocols were approved by the Animal Ethics Committee of Nankai University. To establish tumors in six-week-old BALB/c mice (obtained from the Laboratory Animal Center of the Academy of Military Medical Sciences (Beijing, China)), two million 4T1 cells suspended in 50 mL of 50 $_{v/v}$% mixture of Matrigel in supplemented DMEM (10% fetal bovine serum, 1% pen/strep, 100 U/mL penicillin and 100 µg/mL streptomycin) were injected subcutaneously in the shoulders of the mouse. Tumors were grown until a single aspect was ~7 mm (approximately 10–15 days) before used for PA imaging and PTT experiments.

In Vivo **Photoacoustic Imaging**. After nude mice were anesthetized using 2% isoflurane in oxygen, SPN-F0 (200 µL, 100 µg/mL) (n=4), SPN-F20 (200 µL, 100 µg/mL) (n=4) or saline (200 µL) (n=4) were systematically injected through the tail vein using a microsyringe. Endra Nexus128 PA imaging system was used to acquire the PA images at 750 nm after systematically administration of SPN-F0, SPN-F20 or saline. Data was acquired through a continuous model that took 12 s to obtain one data set. Three dimensional PA image was reconstructed off-line using data acquired from all 128 transducers at each view and a back-projection algorithm. The

algorithm corrects for pulse-to-pulse variations in the laser intensity and small changes in the temperature that affect acoustic velocity in the water.

***In Vivo* Epi-fluorescence Imaging.** Fluorescence whole-animal imaging was performed on a CRi Maestro whole animal imaging system (Caliper Life Sciences, MA, USA). BALB/c mice bearing 4T1 tumors were injected with SPN-F0 (200 μL, 100 μg/mL) (n=4) through tail vein using a microsyringe. Fluorescence imagings of mice were acquired at designated time points after nanoparticle administration. Image quantitation was performed using Nuance software.

***In Vivo* PTT of SPNs**. BALB/c mice bearing 4T1 tumors were exposure to 808 nm laser of 0.3 W/cm^2, after systemic administration of saline (200 μL) (n=4), SPN-F0 (200 μL, 100 μg/mL) (n=4) or SPN-F20 (200 μL, 100 μg/mL) (n=4) at post-injection time of 6 h. Using IR thermal camera to record the temperature change of the tumor in every 15 seconds for 5 minutes after irradiation. The tumor size was measured by caliper every the other day and calculated as the volume= (tumor length) × (tumor width)^2/2. Relative tumor size was calculated as V/V_o (V_o was the initial tumor volume). Mice with tumors larger than 1000 mm^3 should be euthanized according to the standard animal protocol.

Biodistribution Method. After 24 h post-injected with SPN-F0 (200 μL, 100 μg/mL) (n=4) or SPN-F20 (200 μL, 100 μg/mL) (n=4), the mice were sacrificed by CO_2 asphyxiation. Major organs, including liver, kidney, pancreas, heart, brain, skin and spleen were harvested and weighted at 100 mg. The organ parts were embedded in the agar gel and the PA signals were detected under pulsed laser (7 ns pulses, 20 Hz pulse repetition frequency, 9 mJ/pulse) of 750 nm using Endra Nexus128 PA imaging system.

Histological Studies. After 16 days of PTT, the mice treated with SPN-F0 (200 μL, 100 μg/mL) (n=4), SPN-F20 (200 μL, 100 μg/mL) (n=4) and saline (200 μL) (n=4) were sacrificed. The liver,

spleen and tumor were fixed in 4% formalin and then conducted with paraffin embedded section for H&E staining. The superficial and deep regions for tumor tissues were defined as 1 and 4 mm away from the tumor surface, respectively. The slices were examined by a digital microscope (Leica QWin). For proliferating cell nuclear antigen (PCNA) staining, formalin-fixed tumor and organs samples were sliced and used for confocal immunefluorescent analysis using PC10 Mouse mAb (#2586, Cell Signaling Technology) following the supplier's protocol. For the TUNEL apoptosis staining, the fixed tumor sections were determined following manual instruction of In-Situ Cell Death Detection Kit (Roche Applied Science). Hoechst 33342 was used for nuclear counterstaining.

Data Analysis. PA signal intensities were measured by region of interest (ROI) analysis using the Vevo LAZR imaging system software package or OsiriX. PTT graph process was using the software FLIR Tools. Results are expressed as the mean± SD deviation unless otherwise stated. All statistical calculations were performed using GraphPad Prism v.5 (GraphPad Software Inc., CA, USA).

ASSOCIATED CONTENT

Supporting Information

This material is available free of charge *via* the Internet at http://pubs.acs.org.

Supporting Figures S1-10 detail the characterization of the SPNs as well as *in-vitro*, *in-vivo* and *ex-vivo* data.

AUTHOR INFORMATION

Corresponding Author

*Email: kypu@ntu.edu.sg.

Notes

REFERENCES

1. Jokerst, J. V.; Gambhir, S. S. Molecular Imaging with Theranostic Nanoparticles. *Acc. Chem. Res.* 2011, 44, 1050-1060.
2. Pei, H.; Zuo, X. L.; Zhu, D.; Huang, Q.; Fan, C. H. Functional DNA Nanostructures for Theranostic Applications. *Acc. Chem. Res.* 2014, 47, 550-559.
3. Ng, K. K.; Lovell, J. F.; Zheng, G. Lipoprotein-Inspired Nanoparticles for Cancer Theranostics. *Acc. Chem. Res.* 2011, 44, 1105-1113.
4. Liu, J. N.; Bu, W. B.; Shi, J. L. Silica Coated Upconversion Nanoparticles: A Versatile Platform for the Development of Efficient Theranostics. *Acc. Chem. Res.* 2015, 48, 1797-1805.
5. Yu, J.; Ju, Y. M.; Zhao, L. Y.; Chu, X.; Yang, W. L.; Tian, Y. L.; Sheng, F. G.; Lin, J.; Liu, F.; Dong, Y. H.; Hou, Y. L. Multistimuli-Regulated Photochemothermal Cancer Therapy Remotely Controlled *via* Fe_5C_2 Nanoparticles. *ACS Nano* 2015. DOI:10.1021/acsnano.5b04706
6. Ni, D. L.; Zhang, J. W.; Bu, W. B.; Xing, H. Y.; Han, F.; Xiao, Q. F.; Yao, Z. W.; Chen, F.; He, Q. J.; Liu, J. N.; Zhang, S. J.; Fan, W. P.; Zhou, L. P.; Peng, W. J.; Shi, J. L. Dual-Targeting Upconversion Nanoprobes across the Blood–Brain Barrier for Magnetic Resonance/Fluorescence Imaging of Intracranial Glioblastoma. *ACS Nano* 2014, 8, 1231-1242.
7. Fan, W. P.; Shen, B.; Bu, W. B.; Chen, F.; Zhao, K. L.; Zhang, S. J.; Zhou, L. P.; Peng, W. J.; Xiao, Q. F.; Xing, H. Y.; Liu, J. N.; Ni, D. L.; He, Q. J.; Shi, J. L. Rattle-Structured Multifunctional Nanotheranostics for Synergetic Chemo-/Radiotherapy and Simultaneous Magnetic/Luminescent Dual-Mode Imaging. *J. Am. Chem. Soc.* 2013, 135, 6494-6503.
8. Yang, K.; Yang, G. B.; Chen, L.; Cheng, L.; Wang, L.; Ge, C. C.; Liu, Z. FeS Nanoplates as a Multifunctional Nano-Theranostic for Magnetic Resonance Imaging Guided Photothermal Therapy. *Biomaterials* 2015, 38, 1-9.
9. Wang, X.; Niu, D. C.; Li, P.; Wu, Q.; Bo, X. W.; Liu, B. J.; Bao, S.; Su, T.; Xu, H. X.; Wang, Q. G. Dual-Enzyme-Loaded Multifunctional Hybrid Nanogel System for Pathological Responsive Ultrasound Imaging and T_2-Weighted Magnetic Resonance Imaging. *ACS Nano* 2015, 9, 5646-5656.
10. Black, K. C. L.; Wang, Y. C.; Luehmann, H. P.; Cai, X.; Xing, W. X.; Pang, B.; Zhao, Y. F.; Cutler, C. S.; Wang, L. V.; Liu, Y. J.; Xia, Y. N. Radioactive [198]Au-Doped

Nanostructures with Different Shapes for *In Vivo* Analyses of Their Biodistribution, Tumor Uptake, and Intratumoral Distribution. *ACS Nano* 2014, 8, 4385-4394.

11. Su, X. H.; Cheng, K.; Liu, Y.; Hu, X.; Meng, S. X.; Cheng, Z. PET Imaging of Insulin-Like Growth Factor Type 1 Receptor Expression with a ^{64}Cu-Labeled Affibody Molecule. *Amino acids* 2015, 47, 1409-1419.

12. Melancon, M. P.; Zhou, M.; Li, C. Cancer Theranostics with Near-Infrared Light-Activatable Multimodal Nanoparticles. *Acc. Chem. Res.* 2011, 44, 947-956.

13. Wang, L. V.; Hu, S. Photoacoustic Tomography: *In Vivo* Imaging from Organelles to Organs. *Science* 2012, 335, 1458-1462.

14. Zhang, H. F.; Maslov, K.; Stoica, G.; Wang, L. H. V. Functional Photoacoustic Microscopy for High-Resolution and Noninvasive *In Vivo* Imaging. *Nat. Biotechnol.* 2006, 24, 848-851.

15. Wang, L. V. Multiscale Photoacoustic Microscopy and Computed Tomography. *Nat. Photon.* 2009, 3, 503-509.

16. Yu, J.; Yang, C.; Li, J. S.; Ding, Y. C.; Zhang, L.; Yousaf, M. Z.; Lin, J.; Pang, R.; Wei, L. B.; Xu, L. L.; Sheng, F. G.; Li, C. H.; Li, G. J.; Zhao, L. Y.; Hou, Y. L. Multifunctional Fe$_5$C$_2$ Nanoparticles: A Targeted Theranostic Platform for Magnetic Resonance Imaging and Photoacoustic Tomography-Guided Photothermal Therapy. *Adv. Mater.* 2014, 26, 4114-4120.

17. Zerda, A.; Kim, J. W.; Galanzha, E. I.; Gambhir, S. S.; Zharov, V. P. Advanced Contrast Nanoagents for Photoacoustic Molecular Imaging, Cytometry, Blood Test and Photothermal Theranostics. *Contrast Media. Mol. I.* 2011, 6, 346-369.

18. Levi, J.; Kothapalli, S. R.; Ma, T.-J.; Hartman, K.; Khuri-Yakub, B. T.; Gambhir, S. S. Design, Synthesis, and Imaging of an Activatable Photoacoustic Probe. *J. Am. Chem. Soc.* 2010, 132, 11264-11269.

19. Zhang, Y.; Cai, X.; Wang, Y.; Zhang, C.; Li, L.; Choi, S. W.; Wang, L. V.; Xia, Y. N. Noninvasive Photoacoustic Microscopy of Living Cells in Two and Three Dimensions through Enhancement by a Metabolite dye. *Angew. Chem., Int. Ed.* 2011, 123, 7497-7501.

20. Lovell, J. F.; Jin, C. S.; Huynh, E.; Jin, H. L.; Kim, C.; Rubinstein, J. L.; Chan, W. C. W.; Cao, W. G.; Wang, L. V.; Zheng, G. Porphysome Nanovesicles Generated by Porphyrin Bilayers for Use as Multimodal Biophotonic Contrast Agents. *Nat. Mater.* 2011, 10, 324-332.

21. Jin, C. S.; Lovell, J. F.; Chen, J.; Zheng, G. Ablation of Hypoxic Tumors with Dose-Equivalent Photothermal, but Not Photodynamic, Therapy Using a Nanostructured Porphyrin Assembly. *ACS Nano* 2013, 7, 2541-2550.

22. Huynh, E.; Lovell, J. F.; Helfield, B. L.; Jeon, M.; Kim, C.; Goertz, D. E.; Wilson, B. C.; Zheng, G. Porphyrin Shell Microbubbles with Intrinsic Ultrasound and Photoacoustic Properties. *J. Am. Chem. Soc.* 2012, 134, 16464-16467.

23. Ku, G.; Zhou, M.; Song, S. L.; Huang, Q.; Hazle, J.; Li, C. Copper Sulfide Nanoparticles As a New Class of Photoacoustic Contrast Agent for Deep Tissue Imaging at 1064 nm. *ACS Nano* 2012, 6, 7489-7496.

24. Eghtedari, M.; Oraevsky, A.; Copland, J. A.; Kotov, N. A.; Conjusteau, A.; Motamedi, M. High Sensitivity of *In Vivo* Detection of Gold Nanorods Using a Laser Optoacoustic Imaging System. *Nano Lett.* 2007, 7, 1914-1918.

25. Huang, X.; El-Sayed, I. H.; Qian, W.; El-Sayed, M. A. Cancer Cell Imaging and Photothermal Therapy in the Near-Infrared Region by Using Gold Nanorods. *J. Am. Chem. Soc.* 2006, 128, 2115-2120.

26. Kim, J.-W.; Galanzha, E. I.; Shashkov, E. V.; Moon, H.-M.; Zharov, V. P. Golden Carbon Nanotubes as Multimodal Photoacoustic and Photothermal High-Contrast Molecular Agents. *Nat. Nanotech.* 2009, 4, 688-694.

27. Gobin, A. M.; Lee, M. H.; Halas, N. J.; James, W. D.; Drezek, R. A.; West, J. L. Near-Infrared Resonant Nanoshells for Combined Optical Imaging and Photothermal Cancer Therapy. *Nano Lett.* 2007, 7, 1929-1934.

28. Murakami, T.; Nakatsuji, H.; Inada, M.; Matoba, Y.; Umeyama, T.; Tsujimoto, M.; Isoda, S.; Hashida, M.; Imahori, H. Photodynamic and Photothermal Effects of Semiconducting and Metallic-Enriched Single-Walled Carbon Nanotubes. *J. Am. Chem. Soc.* 2012, 134, 17862-17865.

29. Moon, H. K.; Lee, S. H.; Choi, H. C. *In Vivo* Near-Infrared Mediated Tumor Destruction by Photothermal Effect of Carbon Nanotubes. *ACS Nano* 2009, 3, 3707-3713.

30. De La Zerda, A.; Zavaleta, C.; Keren, S.; Vaithilingam, S.; Bodapati, S.; Liu, Z.; Levi, J.; Smith, B. R.; Ma, T.-J.; Oralkan, O.; Cheng, Z.; Chen, X. Y.; Dai, H. J.; Khuri-Yakub, B. T.; Gambhir, S. S. Carbon Nanotubes as Photoacoustic Molecular Imaging Agents in Living Mice. *Nat. Nanotech.* 2008, 3, 557-562.

31. Zerda, A. d. l.; Liu, Z.; Bodapati, S.; Teed, R.; Vaithilingam, S.; Khuri-Yakub, B. T.; Chen, X. Y.; Dai, H. J.; Gambhir, S. S. Ultrahigh Sensitivity Carbon Nanotube Agents for Photoacoustic Molecular Imaging in Living Mice. *Nano Lett.* 2010, 10, 2168-2172.

32. Shi, L.; Cheng, Z. H.; Zhang, J. X.; Li, R.; Zhao, P.; Fu, Z.; You, Y. P. hsa-miR-181a and hsa-miR-181b Function as Tumor Suppressors in Human Glioma Cells. *Brain Res.* 2008, 1236, 185-193.

33. Sheng, Z. H.; Song, L.; Zheng, J. X.; Hu, D. H.; He, M.; Zheng, M. B.; Gao, G. H.; Gong, P.; Zhang, P. F.; Ma, Y. F. Protein-Assisted Fabrication of Nano-Reduced Graphene Oxide for Combined *In Vivo* Photoacoustic Imaging and Photothermal Therapy. *Biomaterials* 2013, 34, 5236-5243.

34. Patel, M. A.; Yang, H.; Chiu, P. L.; Mastrogiovanni, D. D.; Flach, C. R.; Savaram, K.; Gomez, L.; Hemnarine, A.; Mendelsohn, R.; Garfunkel, E.; Jiang, H.; He, H. Direct Production of Graphene Nanosheets for Near Infrared Photoacoustic Imaging. *ACS Nano* 2013, 7, 8147-8157.

35. Nguyen, K. T.; Sreejith, S.; Joseph, J.; He, T. C.; Borah, P.; Guan, E. Y.; Lye, S. W.; Sun, H.; Zhao, Y. L. Poly (Acrylic Acid)-Capped and Dye-Loaded Graphene Oxide-Mesoporous Silica: A Nano-Sandwich for Two-Photon and Photoacoustic Dual-Mode Imaging. *Part. Part. Syst. Char.* 2014, 31, 1060-1066.

36. Akhavan, O.; Ghaderi, E.; Aghayee, S.; Fereydooni, Y.; Talebi, A. The Use of a Glucose-Reduced Graphene Oxide Suspension for Photothermal Cancer Therapy. *J. Mater. Chem.* 2012, 22, 13773-13781.

37. Akhavan, O.; Ghaderi, E. Graphene Nanomesh Promises Extremely Efficient *In Vivo* Photothermal Therapy. *Small* 2013, 9, 3593-3601.

38. Pu, K.; Shuhendler, A. J.; Jokerst, J. V.; Mei, J. G.; Gambhir, S. S.; Bao, Z. N.; Rao, J. H. Semiconducting Polymer Nanoparticles as Photoacoustic Molecular Imaging Probes In Living Mice. *Nat. Nanotech.* 2014, 9, 233-239.

39. Pu, K; Shuhendler, A. J.; Rao, J. H. Semiconducting Polymer Nanoprobe for *In Vivo* Imaging of Reactive Oxygen and Nitrogen Species. *Angew. Chem. Int. Ed.* 2013, 52, 10325-10329.

40. Huang, P.; Lin, J.; Wang, X. S.; Wang, Z.; Zhang, C. L.; He, M.; Wang, K.; Chen, F.; Li, Z. M.; Shen, G. X.; Cui, D. X.; Chen, X. Y. Light-Triggered Theranostics Based on Photosensitizer-Conjugated Carbon Dots for Simultaneous Enhanced-Fluorescence Imaging and Photodynamic Therapy. *Adv. Mater.* 2012, 24, 5104-5110.

41. Shuhendler, A. J.; Pu, K. Y.; Cui, L. N.; Uetrecht, J. P.; Rao, J. H. Real-Time Imaging of Oxidative and Nitrosative Stress in the Liver of Live Animals for Drug-Toxicity Testing. *Nat. Biotechnol.* 2014, 32, 373-380.

42. Pu, K. Y.; Chattopadhyay N.; Rao, J. H. Recent Advance of Semiconducting Polymer Nanoparticles in *in vivo* Molecular Imaging. *J. Control. Release*. 2016, doi: 10.1016/j.jconrel.2016.01.004.

43. Miao, Q. Q.; Lyu, Y.; Ding, D.; Pu, K. Y. Semiconducting Oligomer Nanoparticle as Activatable Photoacoustic Probe with Amplified Brightness for *in vivo* Imaging of pH. *Adv. Mater.* 2016, DOI: 10.1002/adma.201505681, accepted.

44. Xu, L. G.; Cheng, L.; Wang, C.; Peng, R.; Liu, Z. Conjugated Polymers for Photothermal Therapy of Cancer. *Polym. Chem.* 2014, 5, 1573-1580.

45. Wu, C. F.; Schneider, T.; Zeigler, M.; Yu, J. B.; Schiro, P. G.; Burnham, D. R.; McNeill, J. D.; Chiu, D. T. Bioconjugation of Ultrabright Semiconducting Polymer Dots for Specific Cellular Targeting. *J. Am. Chem. Soc.* 2010, 132, 15410-15417.

46. Wu, C. F.; Jin, Y. H.; Schneider, T.; Burnham, D. R.; Smith, P. B.; Chiu, D. T. Ultrabright and Bioorthogonal Labeling of Cellular Targets Using Semiconducting Polymer Dots and Click Chemistry. *Angew. Chem. Int. Ed.* 2010, 49, 9436-9440.

47. Feng, X. L.; Tang, Y. L.; Duan, X. R.; Liu, L. B.; Wang, S. Lipid-Modified Conjugated Polymer Nanoparticles for Cell Imaging and Transfection. *J. Mater. Chem.* 2010, 20, 1312-1316.

48. Howes, P.; Green, M.; Levitt, J.; Suhling, K.; Hughes, M. Phospholipid Encapsulated Semiconducting Polymer Nanoparticles: Their Use in Cell Imaging and Protein Attachment. *J. Am. Chem. Soc.* 2010, 132, 3989-3996.

49. Pu, K; Shuhendler, A. J.; Valta, M. P.; Cui, L. N.; Saar, M.; Peehl, D. M.; Rao, J. H. Phosphorylcholine-Coated Semiconducting Polymer Nanoparticles as Rapid and Efficient Labeling Agents for *In Vivo* Cell Tracking. *Adv. Healthc. Mater.* 2014, 3, 1292-1298.

50. Wu, C. F.; Hansen, S. J.; Hou, Q.; Yu, J. B.; Zeigler, M.; Jin, Y. H.; Burnham, D. R.; McNeill, J. D.; Olson, J. M.; Chiu, D. T. Design of Highly Emissive Polymer Dot Bioconjugates for *In Vivo* Tumor Targeting. *Angew. Chem. Int. Ed.* 2011, 50, 3430-3434.

51. Li, K.; Ding, D.; Huo, D.; Pu, K. Y.; Ngo, N. P. T.; Hu, Y.; Li, Z.; Liu, B. Conjugated Polymer Based Nanoparticles as Dual-Modal Probes for Targeted *In Vivo* Fluorescence and Magnetic Resonance Imaging. *Adv. Funct. Mater.* 2012, 22, 3107-3115.

52. Hong, G. S.; Zou, Y. P.; Antaris, A. L.; Diao, S.; Wu, D.; Cheng, K.; Zhang, X. D.; Chen, C. X.; Liu, B.; He, Y. H.; Wu, J.; Yuan, J.; Zhang, B.; Tao, Z. M.; Fukunaga, C.; Dai, H. J. Ultrafast Fluorescence Imaging *In Vivo* with Conjugated Polymer Fluorophores in the Second Near-Infrared Window. *Nat. Commun.* 2014, 5.

53. Pu, K.; Mei, J. G.; Jokerst, J. V.; Hong, G. S.; Antaris, A. L.; Chattopadhyay, N.; Shuhendler, A. J.; Kurosawa, T.; Zhou, Y.; Gambhir, S. S.; Bao, Z. N.; Rao, J. H. Diketopyrrolopyrrole-Based Semiconducting Polymer Nanoparticles for *In Vivo* Photoacoustic Imaging. *Adv. Mater.* 2015, 27, 5184-5190.

54. Yang K.; Xu H.; Cheng L.; Sun C.; Wang J.; Liu Z. In Vitro and In Vivo Near-Infrared Photothermal Therapy of Cancer Using Polypyrrole Organic Nanoparticles. *Adv. Mater.* 2012, 24 , 5586-5592.

55. Cheng, L.; Yang, K.; Chen, Q.; Liu, Z. Organic Stealth Nanoparticles for Highly Effective *In Vivo* Near-Infrared Photothermal Therapy of Cancer. *ACS Nano* 2012, 6, 5605-5613.

56. Zhang, D.; Wu, M.; Zeng, Y. Y.; Liao, N. S.; Cai, Z. X.; Liu, G.; Liu, X. L.; Liu, J. F. Lipid-Micelles Packaged with Semiconducting Polymer Dots as Simultaneous MRI/Photoacoustic Imaging and Photodynamic/Photo-Thermal Dual-Modal Therapeutic Agents for Liver Cancer. *J. Mater. Chem. B* 2015.

57. Cui, J. B.; Xu, S. Y.; Guo, C.; Jiang, R.; James, T. D.; Wang, L. Highly Efficient Photothermal Semiconductor Nanocomposites for Photothermal Imaging of Latent Fingerprints. *Anal. Chem.* 2015, 87, 11592-11598.

58. Mühlbacher, D.; Scharber, M.; Morana, M.; Zhu, Z.; Waller, D.; Gaudiana, R.; Brabec, C. High Photovoltaic Performance of a Low-Bandgap Polymer. *Adv. Mater.* 2006, 18, 2884-2889.

59. Kim, D. H.; Ayzner, A. L.; Appleton, A. L.; Schmidt, K.; Mei, J. G.; Toney, M. F.; Bao, Z. N. Comparison of the Photovoltaic Characteristics and Nanostructure of Fullerenes Blended with Conjugated Polymers with Siloxane-Terminated and Branched Aliphatic Side Chains. *Chem. Mater.* 2013, 25, 431-440.

60. Gong, X.; Tong, M. H.; Park, S. H.; Liu, M.; Jen, A.; Heeger, A. J. Semiconducting Polymer Photodetectors with Electron and Hole Blocking Layers: High Detectivity in the Near-Infrared. *Sensors-Basel* 2010, 10, 6488-6496.

61. Kroto, H. W.; Heath, J. R.; O'Brien, S. C.; Curl, R. F.; Smalley, R. E. C 60: Buckminsterfullerene. *Nature* 1985, 318, 162-163.

62. Salim, T.; Wong, L. H.; Bräuer, B.; Kukreja, R.; Foo, Y. L.; Bao, Z. N.; Lam, Y. M. Solvent Additives and Their Effects on Blend Morphologies of Bulk Heterojunctions. *J. Mater. Chem.* 2011, 21, 242-250.

63. Braslavsky, S. E.; Heibel, G. E. Time-Resolved Photothermal and Photoacoustic Methods Applied to Photoinduced Processes in Solution. *Chem. Rev.* 1992 , 92 , 1381.

64. Qi, X.Y.; Pu, K.; Li, H.; Zhou, X.Z.; Wu, S.X.; Fan, Q.L.; Liu, B.; Boey, F.; Huang, W.; Zhang, H. Amphiphilic Graphene Composites. *Angew. Chem. Int. Ed.* 2010, 49, 9426–9429.

Table of Contents Graphic